Ruetschi defects decrease the band gap energy in MnO_2 nanosheets

Kideok D. Kwon[1], Keith Refson[2], and Garrison Sposito[1]
[1]Department of Geochemistry, Lawrence Berkeley National Laboratory, Berkeley, CA 94720, USA
[2]STFC Rutherford Appleton Laboratory, Didcot, Oxfordshire OX11 0QX, UK

Manganese oxide nanosheets have emerged recently as attractive materials for a host of potential applications in energy storage, solar cell fabrication, and catalysis.[1-3] Structurally, these compounds are layer-type $Mn(IV)O_2$ comprising stacked sheets of edge-sharing MnO_6 octahedra. An important characteristic of the sheets in all materials synthesized thus far is the presence of cation vacancies ($Mn_{1-x}\square_xO_2$, where $\square_x$ represents a Mn vacancy) whose negative charge is compensated by interlayer metal cations or protons. Vacancies in metal oxides can function as electron donors or acceptors, thereby enhancing material conductivity, [4-7] and a similar role of the vacancies in Mn oxide nanosheets is possible. Here we show, using density functional theory (DFT), that a Mn(IV) vacancy compensated by protons (a Ruetschi defect[8]) introduces new electron donor-like states above the valence bands of Mn oxide nanosheets, thereby reducing the energy gap between occupied and unoccupied electronic states.

Sakai et al.[9] have explored the photoelectrochemical properties of protonated Mn oxide nanosheets prepared by delaminating a product resulting from acid digestion of layer type $K_{0.45}MnO_2$.[1] These protonated nanosheets, derived from a product which contained approximately 3 mol % vacancies ($H_{0.13}[Mn(IV)_{0.97}\square_{0.03}]O_2$, mean Mn oxidation number 3.87[1]), generated photocurrents under visible light radiation ($\lambda < 500$ nm).[9] The band gap energy was estimated to be 2.23 eV from the excitation wavelength dependence of the incident photon-to-electron conversion efficiency, which was 0.16 % at 400 nm for a monolayer film. Sakai et al.[9] speculated that nanosheet thickness (< 1 nm) plays a significant role in facilitating photocurrent generation. Understanding electronic structure near the band gap of Mn oxide nanosheets is clearly essential to developing the full potential of these new materials for harvesting visible light. Our DFT results imply that nanosheet MnO_2 with cation vacancies offers an effective material for utilizing localized *d* electrons in photoinduced electron-transfer reactions.

Protonated Mn vacancies in Mn(IV) oxides are known in the literature as Ruetschi defects.[8] More specifically, the Ruetschi defect is a Mn(IV) vacancy coordinated with four protons on the O ions around the vacancy to form structural OH groups. Balachandran et al.[10] have reviewed the properties of Ruetschi defects and examined their impact on the structures of a number of MnO_2 polymorphs, including a layer type variety. Using DFT with electron correlations accounted for in the generalized gradient approximation, they found that a Ruetschi defect tends to stabilize MnO_2 polymorphs, especially those with more "open" structures, which feature tunnels formed by chains of edge-sharing octahedra linked by shared corners (e.g. ramsdellite[11]). This allows the Ruetschi protons to avoid Mn and one another while bonding covalently with the O atoms near a vacancy site. A similar defect in TiO_2, i.e. a Ti(IV) vacancy charge-compensated with four protons, has also been predicted to be a stable entity.[12] In the present study, we investigated the comparative impact of the Ruetschi defect on the structure and electronic properties of nanosheet MnO_2 bearing 0.033 and 0.125 Mn vacancies per octahedron.

We have geometry-optimized vacancy-free MnO_2 and its supercells containing the Ruetschi defect using DFT with two different electron-correlation methods: local density approximation (LDA) and generalized gradient approximation (GGA). Vacancy-free $Mn(IV)O_2$, which has not yet been synthesized in the laboratory, was optimized starting from the Mn and O atomic coordinates for a microcrystalline layer type MnO_2 prepared by thermal decomposition of $KMnO_4$ at 800°C.[13] This Mn oxide has space group $P6_3/mmc$ and a two-layer unit cell with hexagonal lattice parameters a = 2.840 Å and c =14.031 Å. The Ruetschi defect was incorporated in MnO_2 supercells by coordination of one Mn vacancy at the center of each supercell to four H on dangling O ions around the vacancy (Fig. 1). Two different defect concentrations were modeled, with one Mn vacancy placed in the 4x4x1 (32 Mn atoms) and 2x2x1 (8 Mn atoms) supercells, corresponding to structural formulas, $H_{0.13}[Mn_{0.967}\square_{0.033}]O_2$ and $H_{0.50}[Mn_{0.875}\square_{0.125}]O_2$, respectively. As expected, in both the vacancy-free MnO_2 and the Ruetschi-defected supercells, LDA predicted smaller lattice parameters, as well as shorter Mn-O bond distances, whereas GGA predicted larger values than the available experimental ones[2, 3, 13,14] (Table 1).

In the Ruetschi-defected MnO_2, the four H formed covalent bonds with coordinating O (O_H) (OH distance 0.984 to 1.001 Å) and hydrogen bonds (O-H…O distance 1.96 to 2.17 Å) with O coordinated to two Mn (O_{2Mn}) near the cavity, such that the OH groups were oriented to

make a small angle (4º to 10º) with respect to the *a*-*b* plane (Fig. 1a). The interatomic distances between H are very short: 1.640 Å (LDA) and 1.732 Å (GGA) in the 2x2x1 supercells and 1.773 Å (LDA) and 1.878 Å (GGA) in the 4x4x1 supercells. Possible H arrangements were explored by calculating total energies, with H thereby found to coordinate preferentially with O_{2Mn}, as would be expected from Pauling's rules, and to come into close proximity to one another (Supplementary Figure 1), similar to what was reported by Balachandran et al.[10]

The Ruetschi defect caused considerable local distortion of octahedra near the vacancy site through significant displacements of neighboring O. The O_H moved relatively outward, away from the Mn vacancy along the [111], [-1-11], [11-1], and [-1-1-1] directions, by 0.305 – 0.347 Å in the 4x4x1 supercells and by 0.241 – 0.287 Å in the 2x2x1 supercells, as compared to their positions in vacancy-free MnO_2 (Fig. 1). By contrast, the O_{2Mn} moved relatively inward toward the Mn vacancy along the [1-1-1] and [-111] directions, by 0.108 – 0.072 Å in the 4x4x1 supercells and by 0.089 – 0.084 Å in the 2x2x1 supercells. These atom displacements caused a corrugation of the oxygen surface of the MnO_2 sheet (Supplementary Figure 1) and significantly changed *d*(Mn-Mn) and *d*(Mn-O) near the vacancy sites. However, minor changes were observed in the overall average values for *d*(Mn-Mn) and *d*(Mn-O) (Table 1).

The most prominent structural change that the Ruetschi defect caused is in the thickness of a MnO_2 sheet (i.e., the average distance between basal O planes in a sheet). In vacancy-free MnO_2, both LDA and GGA yielded a smaller MnO_2 sheet thickness than the experimental value (Table 1). Vacancy inclusion increased the sheet thickness by up to 0.1 Å (vacancy-free MnO_2 vs. 2x2x1 supercells), bringing it closer to the experimental result, mainly due to the outward movement of O_H at the Mn vacancy sites. This thickness increase can be seen in the changes of the O-O distances along both shared ($d(O\text{-}O)_{sh}$) and unshared ($d(O\text{-}O)_{ush}$) octahedral edges (see Fig. 1a). An octahedron having O_h point group symmetry has a $d(O\text{-}O)_{sh}/d(O\text{-}O)_{ush}$ ratio equal to 1.0, and deviations of this ratio from 1.0 indicate a trigonally-distorted octahedron, either compressed or elongated. Octahedra in vacancy-free MnO_2 sheets have a ratio of 0.88, which shows a much-compressed form, such that each MnO_6 octahedron takes on a trigonally- distorted symmetry (e.g., point group D_{3d}) instead of perfect O_h symmetry. We observed an increase in the ratio of average $d(O\text{-}O)_{sh}$ to average $d(O\text{-}O)_{ush}$ as the vacancy rate increased (Table 1).

The band structure and partial electronic density of states (PDOS) of the vacancy-free MnO_2 (GGA approximation) are presented in Fig. 2. Because our LDA results were very close to

the GGA results, we mainly describe the latter. The vacancy-free MnO_2 has spin-dependent mixing, mainly between Mn-3*d* and O-2*p* states, with an indirect band gap energy of 1.3 eV. In the spin-up state, the contribution of O to the total DOS was similar to that of Mn throughout. In the spin-down state, however, the O contribution was more significant than the Mn contribution to the valence bands (VB), whereas Mn-3*d* states predominated over O-2*p* states in the conduction bands (CB). The hybridization of O-2*p* states with the spin-polarized Mn-3*d* states leads to exchange splitting of the O-2*p* states. This exchange splitting is reflected in their spin polarization. The calculated magnetic moments in the vacancy-free MnO_2 are -0.04 μ_B for O and 3.08 μ_B for Mn. Spin polarization of *p* states in non-magnetic elements is often observed in *p*-*d* hybridization of ferromagnetic transition metal compounds.[15] In crystal field theory, degenerate 3-*d* states of a transition metal ion split into higher energy e_g (e.g., d_{x2-y2} and d_{z2}) and lower energy t_{2g} (e.g., d_{xy}, d_{yz}, and d_{zx}) states under octahedral coordination. Direct σ-type overlap between the transition metal e_g states and surrounding anion *p* states produces bonding (e_g^b) levels and antibonding (e_g*) levels. In ligand field theory, π-type overlap between t_{2g} states and ligand *p* states can give rise to bonding (t_{2g}^b) levels and antibonding (t_{2g}*) levels. Detailed orbital analysis revealed that the bands around -7 to -5 eV below the Fermi energy (E_F) correspond to bonding dominantly between Mn-e_g states and O-*p* states (i.e., mostly e_g^b levels), whereas the bands from -5 eV to E_F correspond to bonding dominantly between Mn-t_{2g} states and O-*p* states (i.e., mostly t_{2g}^b levels). In particular, the bands between -1.5 to -0.5 eV, consisting of only spin-up Mn-t_{2g} and O-2*p* states, are regarded as occupied bands of the t_{2g}* levels. Perfect high-spin Mn(IV) does not occur because of slight hybridization between spin-down Mn-3*d* and O-2*p* states. A formal configuration of t_{2g}^3-e_g^0 for Mn can be assigned, however, based on the band structure where the three spin-down t_{2g} and two e_g states are all unoccupied, and two spin-up e_g states are unoccupied.

In Ruetschi-defected MnO_2 supercells, the band structure is not as instructive as was observed for the vacancy-free MnO_2. Instead, the formal configuration of Mn atoms in the Ruetschi-defected MnO_2 can be determined based on an apparent relationship between Mn-3*s* splitting and Mn formal valence states (Fig. 3). In X-ray photoelectron spectroscopy (XPS), spectral splitting of Mn-3*s* has been used to identify formal Mn valence states.[16] The Mn-3*s* splitting originates from exchange interactions between Mn-3*s* and Mn-3*d* electrons, as well as from intrashell electron-correlation and charge-transfer effects.[17] According to the DFT

calculations, Mn-3*s* states were strongly polarized, and the splitting between spin-up and spin-down states of Mn-3*s* (ΔE_{Mn3s}) corresponds to the Mn-3*s* spectral splitting measured by XPS. The GGA results underestimate ΔE_{Mn3s}, but in a systematic way when compared to the experimental Mn-3*s* splitting[16, 18, 19] (Fig. 3). The calculated ΔE_{Mn3s} are 3.9 eV for vacancy-free MnO_2 and 3.8 to 4.0 eV for Ruetschi-defected MnO_2. This slight change indicates that the influence of Ruetschi defects on magnetic moments of the Mn atoms around the defect sites is minor and, therefore, the same formal configuration t_{2g}^3-e_g^0 Mn (IV) can be assigned to Mn atoms in the Ruetschi-defected MnO_2.

The PDOS of the Ruetschi-defected MnO_2 (Fig. 4) shows that the Ruetschi defect substantially changes electronic structure near the band gap. Although O-2*p* and Mn-3*d* hybridization occurs similarly to that in vacancy-free MnO_2, it decreases the band gap energy from 1.3 eV to 0.9 eV (GGA) in the 4x4x1 supercell and to 0.3 eV in the 2x2x1 supercell. (It is well known that DFT generally underestimates the band gaps of semiconductors. Improved band gap estimates may be obtained with the DFT+U approach[20] or the screened exchange method[21].) This substantial reduction in band gap is due to the introduction of states at the top of the VB by the Ruteschi defect. When compared to the total DOS of the vacancy-free MnO_2, these newly-introduced states (around -1 eV to E_F) are contributed almost entirely by nearest-neighbor Mn and O atoms around the cation vacancy. In particular, the localized states are mostly O_{2Mn}-*p* states and Mn-3*d* states around the Ruetschi defect (see the inset in Fig. 4). The O_{2Mn}-*p* states are oriented parallel to the axial Mn-O bonds in the MnO_6 octahedra and are a consequence of Mn-O bonds lost by removal of Mn^{4+}, which results in 'dangling' states like the non-bonding states compared to O_H (around -8 eV in Fig. 4) or to the saturated O coordinated with three Mn atoms (O_{3Mn}). The O_{2Mn} states are reflected also in the noticeable induction of spin polarization on the O_{2Mn}, increasing the magnetic moment from -0.04 μ_B to + 0.12 – 0.14 μ_B under GGA.

To the best of our knowledge, the results presented here show for the first time that a Ruetschi defect in nanosheet MnO_2 reduces the energy gap between occupied and unoccupied electronic states relative to a hypothetical defect-free layer-type Mn oxide. Vacancy-free MnO_2 would have an indirect band gap (see Fig. 2) and light absorption would therefore typically be weak. Thus, our finding of band gap energy reduction by a Ruetschi defect suggests that photoinduced electronic transitions by nanosheet MnO_2 can be optimized by the control of defect rates during the synthesis of these materials.

METHODS

All first-principle calculations were performed using CASTEP code[22]. The electron exchange and correlation was treated with LDA and GGA/Perdew, Burke, and Ernzerhof (PBE) functionals[23]. Ultrasoft type pseudopotentials[24] were constructed for Mn and O atoms using the on-the-fly pseudopotential generator implemented in CASTEP. The valence electron configurations were $3s^2 3p^6 3d^5 4s^2$ for Mn and $2s^2 2p^4$ for O. For the Mn pseudopotential, *f* state ($l = 4$) was chosen for a local component, and the number of non-local projector were one for *s* states (3*s* and 4*s*) and two for 3*p* and 3*d*. For the O pseupopontential, *d* state ($l = 3$) was chosen for a local component, and two non-local projectors were used on 2*s* and 2*p*. The core radius of O was 1.0 a.u. for local states and 1.3 a.u. for non-local states, and the radius for Mn was 2.3 a.u. for both local and non-local states. The cut-off wave vectors (q_c) were 411 eV and 490 eV for Mn and O, respectively. The pseudopotentials at a 500 eV cut-off energy with LDA reproduced well the structure and energy data of MnO calculated with all-electron method[25]. For H, the default ultrasoft pseudopotential used was set in the depository of CASTEP. The plane-wave basis sets were expanded up to 500 eV. For the first Brillouin zone, 6x6x2 k-point grids[26] were used without the grid origin offset for the vacancy-free MnO_2 ($P6_3/mmc$). For the Ruetschi defected MnO_2, 5x5x2 and 2x2x1 k-point grids were used for a 2x2x1 supercell and a 4x4x1 supercell, respectively. Tests of PBE on the 6x6x2 (vacancy-free MnO_2) and 5x5x2 (Ruetschi-defected MnO_2) grids with the 500 eV cut-off energy achieved very high convergence of force (0.01 eV/Å or better) and stress (0.01 Gpa or much better) for any Cartesian components of atoms and total energy per formula unit (1.5 meV or much better). Shifting the k-point grid to have a gamma point did not improve the results within the precision of the convergence test on vacancy-free MnO_2.

All calculations were performed with spin polarization of a ferromagnetic ordering between Mn atoms. Our tests on vacancy-free MnO_2 showed that non spin-polarized calculations under both LDA and GGA underestimated structural parameters as much as by 0.1 Å when compared to the corresponding spin-polarized calculations as well as available experimental values. Antiferromagnetic alignment between sheets with the ferromagnetic ordering in each sheet was also tested, but the energy difference was less than the converged energy variability of the currently-used methods. The band gaps of vacancy-free MnO_2 and Ruetschi-defected MnO_2

calculated with the antiferromagnetic alignment were identical to those calculated with the ferromagnetic ordering.

Geometry optimizations were performed with the Broyden, Fletcher, Goldfarb, Shanno (BFGS) procedure[27]. Vacancy-free MnO_2 structures were optimized with all cell parameters and internal ionic positions relaxed. For the Ruetschi-defected supercells, the three unit-cell angles (90º, 90º, and 120º) and the *c*-axis lattice parameters (13.892 Å in LDA and 14.001 Å in PBE) were fixed based on the vacancy-free MnO_2 results, but the *a*-and *b*-axis lattice parameters and all internal ionic positions were relaxed. In geometry optimization, the energy tolerance was 0.000005 eV/atom, and the maximum force and stress tolerance on any component of atoms were 0.01 eV/Å and 0.02 GPa, respectively, for both the vacancy-free MnO_2 and Ruetschi-defected MnO_2. Most residual force and stress values were much less than the tolerance.

Partial density of states (PDOS) and Mulliken analysis[28] were determined by projection of planewave eigenfunctions on to pseudo-atomic basis sets[29]. Spilling parameters (difference between plane-wave eigenfunctions and the projected orbitals) for the PDOS and Mulliken charges were less than 4 % and 0.25 %, respectively. Magnetic moments were obtained from the Mulliken analysis.

Acknowledgements

This research reported in this paper was supported by the Director, Office of Energy Research, Office of Basic Energy Sciences, of the U.S. Department of Energy under Contract No. DE-AC03-76SF00098. Our computations used resources of the National Energy Research Scientific Computing Center, which is supported by the Office of Science of the U.S. Department of Energy under contract No. DE-AC02-05CH11231. We also acknowledge the use of the SCARF computing facilities at STFC.

References

1. Omomo, Y., Sasaki, T., Wang, L.Z. & Watanabe, M. Redoxable nanosheet crystallites of MnO_2 derived via delamination of a layered manganese oxide. *J. Am. Chem. Soc.* **125**, 3568-3575 (2003).
2. Fukuda, K. et al. Structure analysis of exfoliated unilamellar crystallites of manganese oxide nanosheets. *J. Phys. Chem. B* **110**, 17070-17075 (2006).
3. Kadoma, Y., Uchimoto, Y. & Wakihara, M. Synthesis and structural study on MnO_2 nanosheet material by X-ray absorption spectroscopic technique. *J. Phys. Chem. B* **110**, 174-177 (2006).
4. Justicia, I. et al. Designed self-doped titanium oxide thin films for efficient visible-light photocatalysis. *Advanced Materials* **14**, 1399-1402 (2002).
5. Elfimov, I.S., Yunoki, S. & Sawatzky, G.A. Possible path to a new class of ferromagnetic and half-metallic ferromagnetic materials. *Phys. Rev. Lett.* **89**, 216403 (2002).
6. Hwang, H.Y. Perovskites - Oxygen vacancies shine blue. *Nat. Mater.* **4**, 803-804 (2005).
7. Nolan, M. & Elliott, S.D. The p-type conduction mechanism in Cu_2O: a first principles study. *Phys. Chem. Chem. Phys.* **8**, 5350-5358 (2006).
8. Ruetschi, P. Cation-vacancy model for MnO_2. *J. Electrochem. Soc.* **131**, 2737-2744 (1984).
9. Sakai, N., Ebina, Y., Takada, K. & Sasaki, T. Photocurrent generation from semiconducting manganese oxide nanosheets in response to visible light. *J. Phys. Chem. B* **109**, 9651-9655 (2005).
10. Balachandran, D., Morgan, D., Ceder, G. & van de Walle, A. First-principles study of the structure of stoichiometric and Mn-deficient MnO_2. *J. Solid State Chem.* **173**, 462-475 (2003).
11. Post, J.E. Manganese oxide minerals: Crystal structures and economic and environmental significance. *Proc. Natl. Acad. Sci. U. S. A.* **96**, 3447-3454 (1999).
12. Grey, I.E. & Wilson, N.C. Titanium vacancy defects in sol-gel prepared anatase. *J. Solid State Chem.* **180**, 670-678 (2007).
13. Gaillot, A.C. et al. Structure of synthetic K-rich birnessite obtained by high-temperature decomposition of $KMnO_4$. I. Two-layer polytype from 800 °C experiment. *Chem. Mater.* **15**, 4666-4678 (2003).
14. Villalobos, M., Lanson, B., Manceau, A., Toner, B. & Sposito, G. Structural model for the biogenic Mn oxide produced by *Pseudomonas putida*. *Am. Mineral.* **91**, 489-502 (2006).
15. Kanamori, J. & Terakura, I. A general mechanism underlying ferromagnetism in transition metal compounds. *J. Phys. Soc. Jpn.* **70**, 1433-1434 (2001).
16. Foord, J.S., Jackman, R.B. & Allen, G.C. An X-ray photoelectron spectroscopic investigation of the oxidation of manganese. *Philos. Mag. A* **49**, 657-663 (1984).
17. Oh, S.J., Gweon, G.H. & Park, J.G. Origin of 3*s* splitting in the photoemission spectra of Mn and Fe insulating compounds. *Phys. Rev. Lett.* **68**, 2850-2853 (1992).

18. Wertheim, G.K., Hüfner, S. & Guggenhe.Hj. Systematics of core-electron exchange splitting in 3*d*-group transition-metal compounds. *Phys. Rev. B* **7**, 556-558 (1973).
19. Galakhov, V.R. et al. Mn 3s exchange splitting in mixed-valence manganites. *Phys. Rev. B* **65**, 113102 (2002).
20. Anisimov, V.I., Aryasetiawan, F. & Lichtenstein, A.I. First-principles calculations of the electronic structure and spectra of strongly correlated systems: The LDA+U method. *J. Phys. Condens. Matter* **9**, 767-808 (1997).
21. Seidl, A., Görling, A., Vogl, P., Majewski, J.A. & Levy, M. Generalized Kohn-Sham schemes and the band-gap problem. *Phys. Rev. B* **53**, 3764-3774 (1996).
22. Clark, S.J. et al. First principles methods using CASTEP. *Z. Kristallogr.* **220**, 567-570 (2005).
23. Perdew, J.P., Burke, K. & Ernzerhof, M. Generalized gradient approximation made simple. *Phys. Rev. Lett.* **77**, 3865-3868 (1996).
24. Vanderbilt, D. Soft self-consistent pseudopotentials in a generalized eigenvalue formalism. *Phys. Rev. B* **41**, 7892-7895 (1990).
25. Pask, J.E., Singh, D.J., Mazin, I.I., Hellberg, C.S. & Kortus, J. Structural, electronic, and magnetic properties of MnO. *Phys. Rev. B* **64**, 024403 (2001).
26. Monkhorst, H.J. & Pack, J.D. Special points for Brillouin-zone Integrations. *Phys. Rev. B* **13**, 5188-5192 (1976).
27. Pfrommer, B.G., Cote, M., Louie, S.G. & Cohen, M.L. Relaxation of crystals with the quasi-Newton method. *J. Comput. Phys.* **131**, 233-240 (1997).
28. Mulliken, R.S. Electronic population analysis on LCAO-MO molecular wave functions .1. *J. Chem. Phys.* **23**, 1833-1840 (1955).
29. Segall, M.D., Shah, R., Pickard, C.J. & Payne, M.C. Population analysis of plane-wave electronic structure calculations of bulk materials. *Phys. Rev. B* **54**, 16317 (1996).

Figure legends

Figure 1 Geometry-optimized structures of (a) the Ruetschi defect supercell 4x4x1 and (b) its middle sheet containing the Ruetschi defect projected onto the *a*-*b* plane.

Figure 2 PBE results for (a) the vacancy-free MnO_2 band structure and (b) its PDOS showing contributions of O-2*p* and Mn-3*d* states. The Fermi energy was set to zero in (a).

Figure 3 Calculated Mn-3*s* splitting (ΔE_{Mn3s}) for Mn atoms in MnO, $LiMnO_2$, vacancy-free MnO_2, and Ruetschi-defected MnO_2. Experimental data are for MnO, Mn_2O_3, and β-MnO_2 (refs 16,18) and MnO, Mn_3O_4, $LiMnO_2$, and Li_2MnO_3 (ref. 19).

Figure 4 Contribution of the Ruetschi defect to the total DOS in (a) the 4x4x1 supercell (0.033 Mn vacancy per octahedron) and (b) the 2x2x1 supercell (0.125 Mn vacancy per octahedron). The Fermi energy (E_F) was set to zero. Note that slight occupation over E_F in the valence bands is due to Gaussian-smearing of the DOS at the 0.05 eV width. For comparison, the total DOS of the vacancy-free MnO_2 supercells was aligned by the minimum of the conduction bands. The atoms around the Mn vacancy are nearest-neighbors of the missing Mn atom: 4 H, 6 O, and 6 Mn atoms (see Fig. 1b). The inset is a perspective view of spin-up orbital densities corresponding to the topmost valence bands on the 0.005 $e^-/Å^3$ isosurface of the 4x4x1 supercell (PBE). The bands consist of mostly Mn-t_{2g} states and O-p_z like (in local coordinates) states at O_{2Mn}.

Figure 1

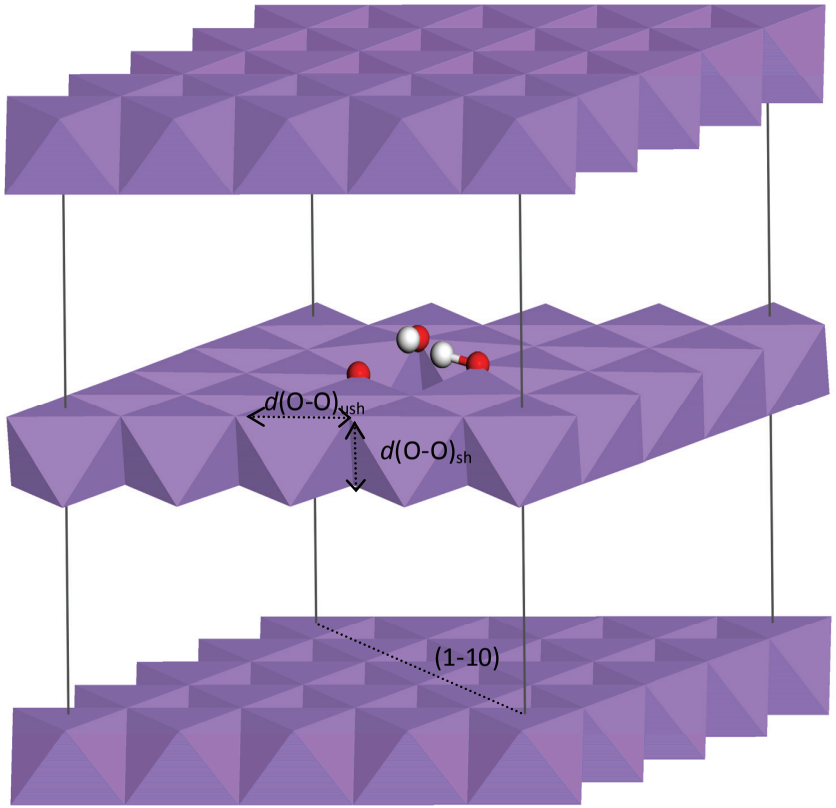

(a)

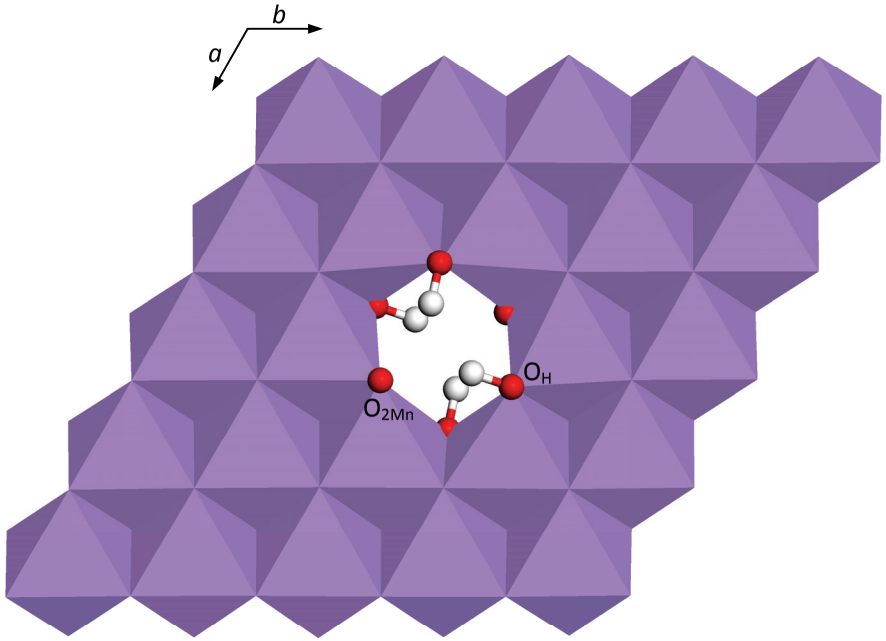

(b)

Figure 2

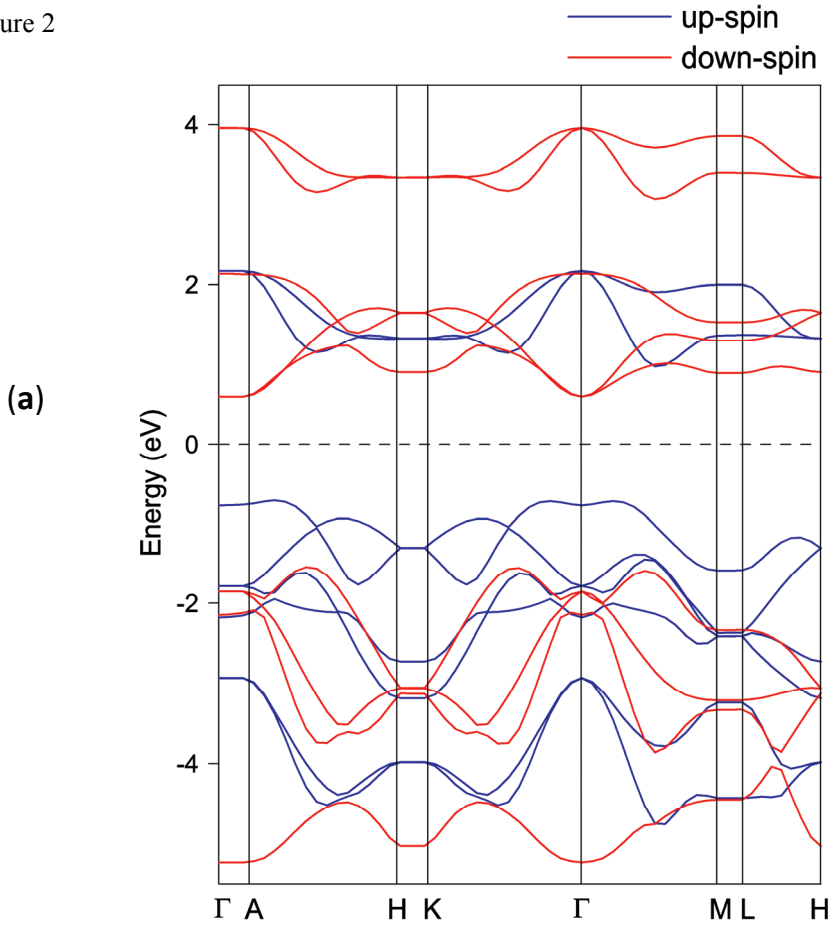
(a)
up-spin
down-spin
Energy (eV)
4
2
0
-2
-4
Γ A H K Γ M L H

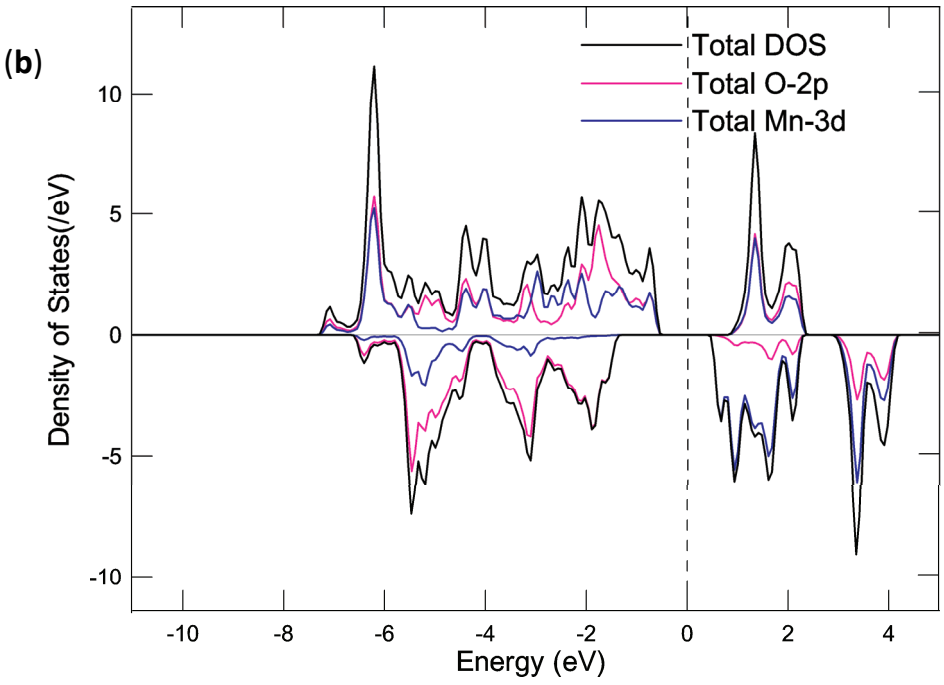
(b)
Total DOS
Total O-2p
Total Mn-3d
Density of States(/eV)
10
5
0
-5
-10
-10 -8 -6 -4 -2 0 2 4
Energy (eV)

Figure 3

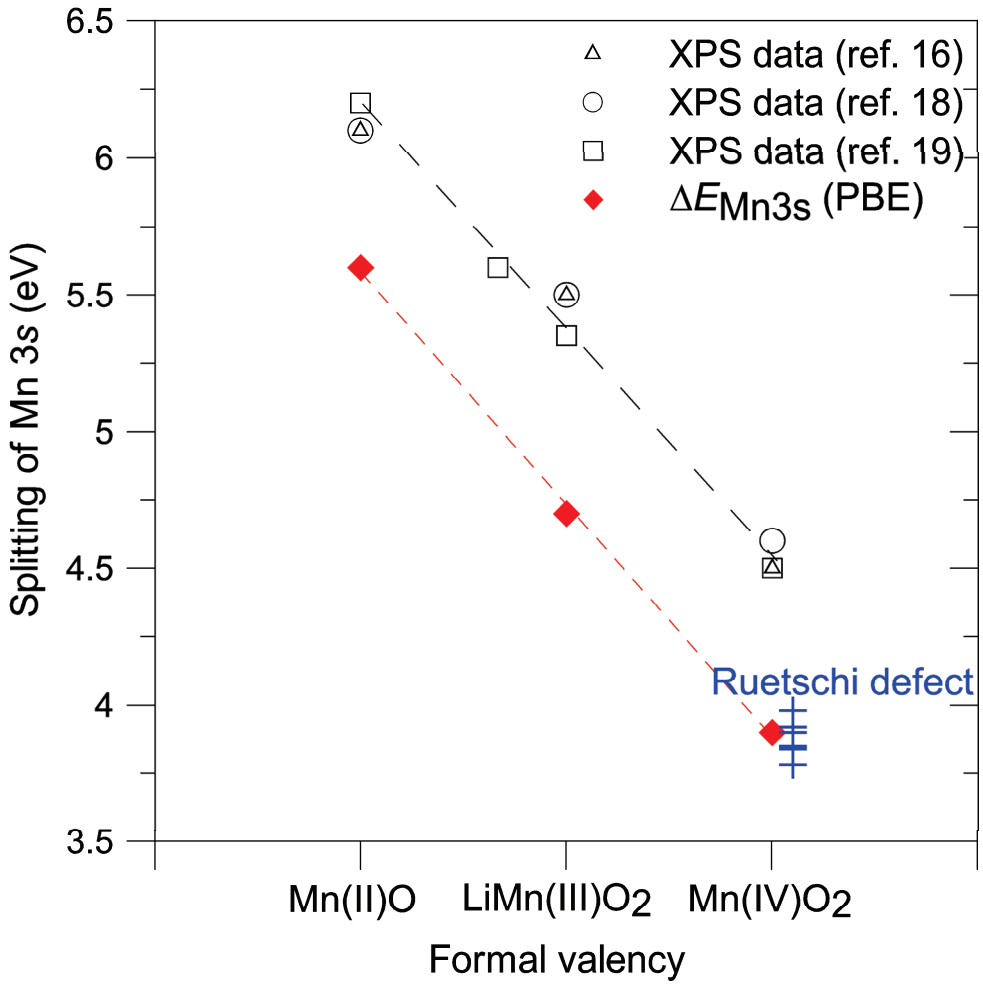
6.5
6
5.5
5
4.5
4
3.5
Splitting of Mn 3s (eV)
XPS data (ref. 16)
XPS data (ref. 18)
XPS data (ref. 19)
ΔEMn3s (PBE)
Ruetschi defect
Mn(II)O
LiMn(III)O2
Mn(IV)O2
Formal valency

Figure 4

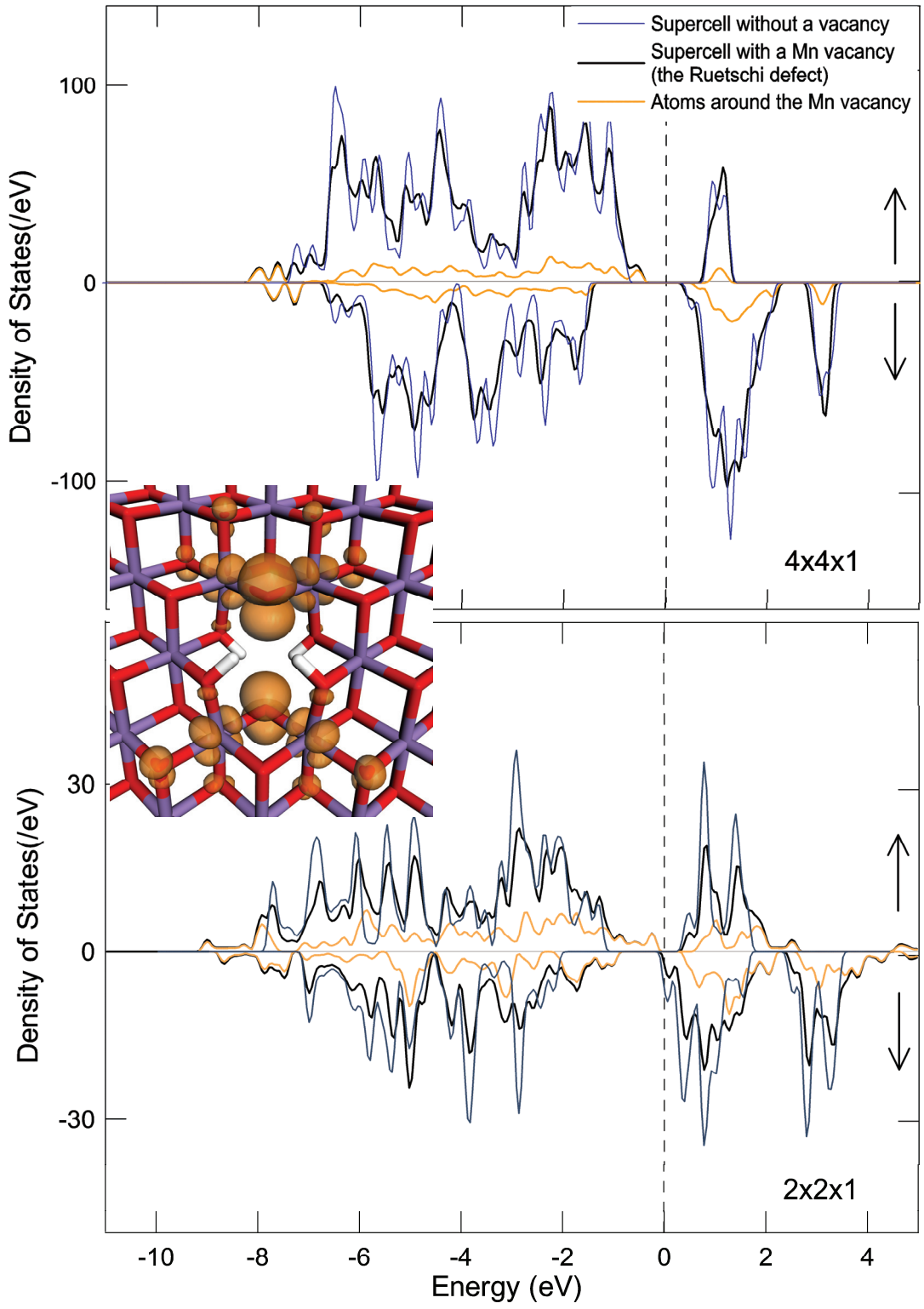
Supercell without a vacancy
Supercell with a Mn vacancy
(the Ruetschi defect)
Atoms around the Mn vacancy
Density of States(/eV)
100
0
-100
4x4x1
30
0
-30
2x2x1
-10
-8
-6
-4
-2
0
2
4
Energy (eV)

Table 1 Interatomic distances in vacancy-free and Ruetschi-defected MnO_2 optimized with DFT under LDA or GGA/PBE.

	LDA			GGA/PBE			Experimental			
Distance (Å)	0.000	0.033	0.125	0.000	0.033	0.125	0.03[a]	0.03[b]	0.06[c]	0.12[d]
Mn_{layer}-Mn_{layer}	2.827	2.756-2.888 (2.825)	2.815	2.897	2.820-2.943 (2.895)	2.895	2.85	2.86	2.88	2.840
Mn_{laye}-O_{layer}	1.883	1.833-1.929 (1.882)	1.854-1.929 (1.882)	1.925	1.852-2.002 (1.928)	1.887-1.979 (1.931)	1.91	1.89	1.90	1.914
Mn sheet thickness	1.88	1.91	1.98	1.91	1.94	2.02				1.96
O-O_{sh}/O-O_{ush}[e]	0.88	0.90	0.93	0.88	0.89	0.91			0.86	0.90

Vacancy rate per octahedron indicated at the top of each column of data. Values in parentheses are averaged interatomic distances. The *c*-axis lattice parameters of the vacancy-free MnO_2 were 13.892 Å (LDA) and 14.001 Å (GGA/PBE). The supercells 4x4x1 and 2x2x1 correspond to $H_{0.13}[Mn_{0.967}\square_{0.033}]O_2$ and $H_{0.50}[Mn_{0.875}\square_{0.125}]O_2$, respectively.

[a]Mn K-edge EXAFS analysis (± 0.01 Å) of protonated nanosheet MnO_2, $H_{0.13}[Mn(IV)_{0.97}\square_{0.03}]O_2{\cdot}0.7H_2O$.[2] The Mn-Mn distance is 2.842 Å by XRD analysis.

[b]Mn K-edge EXAFS analysis of protonated nanosheet MnO_2.[3]

[c]Mn K-edge EXAFS analysis (± 0.02 Å) of nanoparticle δ-MnO_2 with structural formula, $Na_{0.24}[Mn(IV)_{0.94}\square_{0.06}]O_2{\cdot}072H_2O$.[14] The Mn-O distance is 1.92 Å by XRD analysis.

[d]XRD analysis of microcrystalline layer type K-MnO_2 with the structural formula, $K_{0.231}Mn(III)_{0.077}[Mn(IV)_{0.885}\square_{0.115}]O_2{\cdot}0.60H_2O$.[13] The Mn-Mn distance for a powder sample was 2.845 Å by XRD analysis and 2.87 Å by Mn K-edge EXAFS analysis.

[e]Unitless ratio of average distance along shared (O-O_{sh}) and unshared (O-O_{ush}) octahedral edges. Undistorted octahedra yield 1.00.

Supplementary Information

Figure S1. Optimized structures of the Ruetschi defects with different H positions in the 2x2x1 supercell (PBE): (a) H with OH nearly parallel to the *a*-*b* plane, (b) H with OH perpendicular to the sheet, and (c) *cis*-form and (d) *trans*-form between top and bottom OH in a cavity. $E_{tot,r}$ is a total energy relative to the energy of (a) structure.